

## RESEARCH ARTICLE

10.1029/2017JB015349

## Key Points:

- Magnesiowüstite is proposed as a major contributor to the seismic anisotropy detected at the bottom of the mantle
- High-energy resolution inelastic X-ray scattering experiments conducted on magnesiowüstite single crystals at high pressure indicate that its shear anisotropy strongly increases with pressure
- At lower-mantle pressures, the shear anisotropy of magnesiowüstite may be as much as a factor of 2 to 3 higher than postperovskite

## Supporting Information:

- Supporting Information S1

## Correspondence to:

G. J. Finkelstein and J. M. Jackson,  
gjfinkel@hawaii.edu;  
jackson@gps.caltech.edu

## Citation:

Finkelstein, G. J., Jackson, J. M., Said, A., Alatas, A., Leu, B. M., Sturhahn, W., & Toellner, T. S. (2018). Strongly anisotropic magnesiowüstite in Earth's lower mantle. *Journal of Geophysical Research: Solid Earth*, 123, 4740–4750. <https://doi.org/10.1029/2017JB015349>

Received 12 DEC 2017

Accepted 13 MAY 2018

Accepted article online 18 MAY 2018

Published online 16 JUN 2018

## Strongly Anisotropic Magnesiowüstite in Earth's Lower Mantle

Gregory J. Finkelstein<sup>1,2</sup> , Jennifer M. Jackson<sup>1</sup> , Ayman Said<sup>3</sup>, Ahmet Alatas<sup>3</sup> , Bogdan M. Leu<sup>3,4</sup>, Wolfgang Sturhahn<sup>1</sup> , and Thomas S. Toellner<sup>3</sup>

<sup>1</sup>Division of Geological and Planetary Sciences, Caltech, Pasadena, CA, USA, <sup>2</sup>Now at Hawai'i Institute of Geophysics and Planetology, University of Hawai'i at Manoa, Honolulu, HI, USA, <sup>3</sup>Advanced Photon Source, Argonne National Laboratory, Argonne, IL, USA, <sup>4</sup>Now at Department of Physics, Miami University, Oxford, OH, USA

**Abstract** The juxtaposition of a liquid iron-dominant alloy against a mixture of silicate and oxide minerals at Earth's core-mantle boundary is associated with a wide range of complex seismological features. One category of observed structures is ultralow-velocity zones, which are thought to correspond to either aggregates of partially molten material or solid, iron-enriched assemblages. We measured the phonon dispersion relations of (Mg,Fe)O magnesiowüstite containing 76 mol % FeO, a candidate ultralow-velocity zone phase, at high pressures using high-energy resolution inelastic X-ray scattering. From these measurements, we find that magnesiowüstite becomes strongly elastically anisotropic with increasing pressure, potentially contributing to a significant proportion of seismic anisotropy detected near the base of the mantle.

## 1. Introduction

The lower mantle plays a fundamental role in the thermal and chemical evolution of the planet. The boundary between the core and mantle is a primary interface within the deep interior and has a major influence on the cooling of the planet. Seismologists have shown that the mantle side of this boundary is extraordinarily complex, with kilometer-scale fine structure embedded within larger layers of variable size and character. A combination of thermal and chemical heterogeneity, solid-solid phase transitions, anisotropy, complex rheology, and melting is likely required to explain the observed features (Frost et al., 2018; 2017; Li et al., 2017; B. Zhang et al., 2018).

The largest-scale structures in the lower mantle are the African and Pacific large low-shear-velocity provinces (LLSVPs). Recent studies have shown evidence for significant seismic anisotropy near the edges of these structures (Cottaar & Romanowicz, 2013; Ford et al., 2015; Lynner & Long, 2014), which may be generated by solid-state mantle convection (McNamara et al., 2002). The preferential alignment of postperovskite crystals has been implicated as the source of such seismic anisotropy (Ford et al., 2015; Miyagi et al., 2010; Oganov et al., 2005; Wu et al., 2017). However, the core-mantle boundary (CMB) region may also host more chemically complex phase assemblages that are enriched in elements such as iron, aluminum, calcium, and hydrogen (Dorfman & Duffy, 2014; Hirose, 2006; Knittle & Jeanloz, 1986; Mao et al., 2004; Sakai et al., 2009; Shim, 2008; Townsend et al., 2016; Wicks et al., 2010; Williams & Garnero, 1996). Due to their enhanced density and decreased wave velocities, iron-rich systems are thought to be at least partially responsible for explaining ultralow-velocity zones (ULVZs; Garnero & Helmberger, 1995, 1998; Yu & Garnero, 2018).

Crucial to the interpretation of the seismic observations are the material properties of candidate lower-mantle phases. In general, significant progress has been made in determining thermoelastic and chemical properties of relevant phase assemblages and the impact of these properties on lower-mantle dynamics and seismic interpretations. Very low isotropic sound velocities were measured in (Mg<sub>0.16</sub>Fe<sub>0.84</sub>)O at high pressure, suggesting that the presence of iron-rich (Mg,Fe)O can explain the characteristic sound speeds of LVZ and ULVZ near Earth's CMB (Bower et al., 2011; Wicks et al., 2010; 2017). While recent progress has been made in experimentally determining the single-crystal elastic properties and behavior of iron-poor (Mg,Fe)O at high pressures using inelastic X-ray scattering (Antonangeli et al., 2011), impulsive stimulated scattering (Crowhurst et al., 2008), ultrasonic interferometry (Jacobsen et al., 2002, 2004), and Brillouin spectroscopy (J. M. Jackson et al., 2006; Marquardt et al., 2009; Sinogeikin & Bass, 2000), and it has been reported that the elastic anisotropy of (Mg,Fe)O may scale with iron content at high pressures (Marquardt et al., 2009),

no measurements currently exist that constrain the elastic anisotropy of iron-rich  $\text{Mg}_{x-1}\text{Fe}_x\text{O}$  with  $x > 0.17$  at high pressures.

We have conducted momentum-resolved high-energy resolution inelastic X-ray (HERIX) scattering and single-crystal X-ray diffraction (XRD) on single-crystal magnesiowüstite (with 76 mol % FeO) at pressures of Earth's lower mantle and confirmed their reliability by conducting similar measurements on MgO at ambient conditions. Our results show that magnesiowüstite develops strong elastic anisotropy at high pressures and, consequently, may be a source of observable seismic anisotropy.

## 2. Methods

### 2.1. Inelastic X-Ray Scattering, XRD

High-energy resolution momentum-resolved inelastic X-ray scattering (HERIX) and XRD experiments were conducted on single crystals of synthetic MgO and  $(\text{Mg}_{0.215}\text{Fe}_{0.762}\square_{0.023})\text{O}$  magnesiowüstite (Mw) at the ID-C beamline of Sector 30 at the Advanced Photon Source (APS), Argonne National Laboratory (Said et al., 2011; Sinn, 2001; Toellner et al., 2011). The MgO crystal, with face normal [100], was purchased from MTI Corporation and used to benchmark the (Mg,Fe)O measurements. See Jacobsen et al. (2002) and Finkelstein et al. (2017) for details on the synthesis and characterization of the Mw sample.

For measurements at ambient conditions, a  $5 \times 5 \times 0.5\text{-mm}^3$  MgO single-crystal platelet was mounted on a metal post, and a  $\sim 85 \times 40 \times 40\text{-}\mu\text{m}^3$  Mw single crystal was mounted on a MiTeGen MicroMesh™. The Mw crystal was a cleavage fragment with face normal [100], which was confirmed by single-crystal diffraction on a four-circle Bruker D8 Venture diffractometer using a Mo X-ray source at the Caltech X-Ray Crystallography Facility. For high-pressure experiments, a BX90 diamond anvil cell (DAC), utilizing 300- $\mu\text{m}$  culet Boehler-Almax-geometry diamonds and seats for a wide  $\sim 70^\circ$  X-ray opening angle, was used to achieve pressure (Boehler & De Hantsetters, 2007; Kantor et al., 2012). A face normal [100] Mw single-crystal cleavage fragment  $\sim 60 \times 50\text{ }\mu\text{m}$  in diameter and  $\sim 15\text{-}\mu\text{m}$  thick was loaded in a rhenium gasket preindented to a thickness of  $\sim 50\text{ }\mu\text{m}$ , with an initial sample chamber  $\sim 165\text{ }\mu\text{m}$  in diameter. Two ruby spheres  $\sim 10\text{-}\mu\text{m}$  thick were also placed in the sample chamber in order to determine the approximate pressure. The prepared DAC (Figure S2 in the supporting information) was gas loaded with a helium pressure medium to 1.7 kbar using the Caltech gas-loading system. The crystal orientation was confirmed by single-crystal diffraction at Sector 30 before collecting HERIX spectra. Measurements at six pressures (in addition to ambient) were collected, reaching a maximum of 41.2(1.3) GPa. Final pressures were determined by inputting the measured lattice parameters into the previously determined Mw equation of state (Finkelstein et al., 2017).

An incident X-ray energy of 23.7236 keV ( $\lambda = 0.52262\text{ }\text{\AA}$ ), with a full width at half maximum energy resolution of 1 meV, was achieved using a highly efficient, cryogenically stabilized six-reflection monochromator (Said et al., 2011; Toellner et al., 2011). The X-rays were focused onto the sample with a full width at half maximum beam size of  $\sim 15 \times 35\text{ }\mu\text{m}^2$ . An online image plate diffraction detector was used to confirm orientation and orient the crystals with the (200) and (220) Bragg reflections aligned in the horizontal plane. These two reflections were used to determine the crystal's orientation matrix and lattice parameters. The sample density as a function of pressure was calculated from a combination of the unit cell volume corresponding to these lattice parameters with the predetermined sample composition. The photons scattered from the sample were collected and analyzed using a spherically bent silicon crystal analyzer of the (12 12 12) reflection and a detector working very close to back reflection ( $89.98^\circ$ ) in energy ranges as narrow as  $-10$  to  $+15$  meV and as wide as  $\pm 60$  meV for MgO, with a step size of 0.5 meV. The momentum resolution was about  $0.2\text{ nm}^{-1}$ . The collection time for each energy scan ranged from approximately 10 to 50 min and typically 3–4 spectra (but up to a maximum of 5) were added for each point on the dispersion curve using the PADD module in PHOENIX (Sturhahn, 2017). Approximate pressures were determined offline using ruby fluorescence, however the final pressures that we report are based upon the equation of state (EOS) of Mw (Finkelstein et al., 2017).

### 2.2. Synchrotron Mössbauer Spectroscopy

Synchrotron Mössbauer spectra (SMS) were collected in the 24-bunch fill top-up mode at APS Sector 3, beamline ID-B, on a single crystal of Mw with face normal [100] at 12 pressure points between 1 and 64 GPa. The  $\sim 30 \times 30 \times < 10\text{-}\mu\text{m}^3$  crystal was loaded with two  $< 10\text{-}\mu\text{m}$  ruby spheres in a standard symmetric DAC using a  $\sim 40\text{-}\mu\text{m}$ -thick rhenium gasket with an initial sample chamber diameter of  $\sim 130\text{ }\mu\text{m}$ . A helium pressure

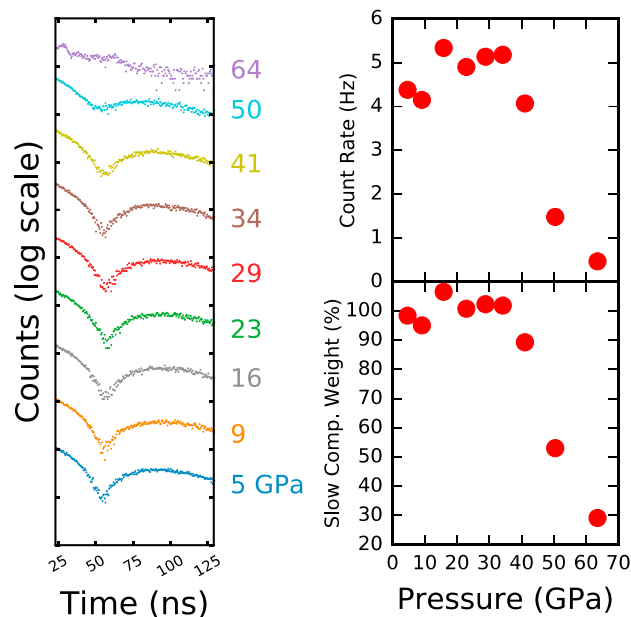


**Figure 1.** (left) Time domain synchrotron Mössbauer spectra of magnesiowüstite as a function of pressure. At 64 GPa, the appearance of high-frequency oscillations in the spectrum indicates a magnetic-ordering transition. (top right) Count rates determined for the time window 23 to 129 ns. (bottom right) Percent proportion of the slow component in the Mössbauer spectra as a function of pressure.

medium was gas loaded using the Caltech system, thus achieving a similar sample environment as the HERIX (this study) and single-crystal XRD measurements of Mw (Finkelstein et al., 2017). Beveled 250- $\mu\text{m}$  culet diamonds epoxied to tungsten carbide seats were used to apply pressure. Pressure in the sample chamber was determined using ruby fluorescence (Dewaele et al., 2004).

For SMS measurements, X-rays were focused on the sample to a spot size of  $\sim 15 \times 18 \mu\text{m}^2$ . An avalanche photodiode detector was used to collect the photons in the forward direction between delay times of 23 and 129 ns. Collection times ranged from  $\sim 2$  to 4 hr depending on the count rate at a given pressure.

### 3. Results

#### 3.1. SMS—Magnesiowüstite

The SMS spectrum at 5 GPa is qualitatively similar in the overlapping time range as one collected at ambient pressure during the hybrid timing mode of the APS, where there is access to longer delay times and thus higher spectral (energy) resolution. In this hybrid-mode spectrum, four unique iron environments could be identified (Finkelstein et al., 2017). The spectra are virtually unchanged up to 34 GPa (Figure 1, left). At higher pressures, a decrease in the delayed forward scattered intensities is observed in the accessible time window.

There are three factors that could cause the decrease in intensity: strong thinning of the sample, a significant drop in the Lamb-Mössbauer factor, or the occurrence of a very fast component in the time spectrum. We can rule out the first two factors, as the sample shape remains unchanged (Figure S1), and nuclear resonant inelastic X-ray scattering experiments on similar compositions did not show a significant decrease in the Lamb-Mössbauer factor (Wicks et al., 2017). By the time our detector has recovered from the intense prompt synchrotron radiation pulse at about 22 ns, this fast component has mostly decayed, leaving no observable trace in the shape of the time spectrum. However, the absence of scattering strength still causes a reduced counting rate (Figure 1, top right). We model this behavior using the concept of effective thickness,  $\eta$ , for nuclear forward scattering (Sturhahn, 2004). The effective thickness is proportional to the concentration of resonant isotope, the Lamb-Mössbauer factor, and physical thickness. Our sample is dilute in the resonant isotope  $^{57}\text{Fe}$ , and the resulting small effective thickness causes the delayed forward scattered intensity to be proportional to  $\eta^2$ . The observed time spectrum only reflects the slow component with weight  $w$ , leading to an intensity proportional to  $w^2$ . Figure 1 (bottom right) shows this weight as a function of pressure, where

$$w = \sqrt{\frac{I_p}{I_0} \frac{F_{LM0}}{F_{LMp}}}$$

with intensities  $I$  from this study and Lamb-Mössbauer factors  $F_{LM}$  taken from Wicks et al. (2017). The  $p$  subscript indicates values that correspond to a pressurized sample and the 0 subscript indicates normalized values that were obtained by averaging intensities/L-M factors up to 34 GPa. At pressures above 34 GPa, a decrease in the weight of the slow component in the time spectrum indicates that one or more sites have developed a very broad energy spectrum. At 64 GPa, fast oscillations are detectable and are indicative of magnetic ordering.

#### 3.2. Inelastic X-Ray Scattering—Spectral Fitting, MgO

All sample crystals were oriented with the surface normal parallel to the [100] direction, thus permitting measurements of the longitudinal acoustic phonon branch along the [100] direction and the transverse acoustic (TA) phonon branches along the [010] and [110] (following the [1-10] polarization) directions. Phonon

branches were measured for at least two different momentum transfers at each pressure point and at a maximum, up to the Brillouin zone edge, in the case of the MgO [100] TA branch. Minimum momentum transfers were chosen to be as close to the Brillouin zone center as possible. Spectral fitting was done using the PyMC3 Markov chain Monte Carlo Python module with the No-U-Turn Sampler (Salvatier et al., 2016). Due to the limited number of points measured along each phonon branch, spectra along a branch at a given pressure were fit simultaneously by putting a strong prior (Gaussian distribution with a standard deviation of 0.05 m/s) on the phonon energies such that they were constrained to lie along the sine function:

$$\text{phonon energy position, } E \text{ [meV]} = 4.192 \times 10^{-4} \times \text{velocity}_{\text{fit}} \left[ \frac{\text{m}}{\text{s}} \right] \times Q_{\text{max}} [\text{nm}^{-1}] \times \sin \left( \frac{\pi Q_{\text{current}} [\text{nm}^{-1}]}{2 Q_{\text{max}} [\text{nm}^{-1}]} \right), \quad (1)$$

which has been discussed in detail in previous studies (e.g., Fiquet et al., 2009; Sakamaki et al., 2016). The two fitting parameters correspond to the approximate sound velocity (in m/s) and location of the Brillouin zone edge (in  $\text{nm}^{-1}$ ).  $Q_{\text{current}}$  is the momentum transfer corresponding to a given spectrum. The velocity parameter was fit using a flat prior, but a strong prior (Gaussian distribution with a standard deviation of  $0.1 \text{ nm}^{-1}$ ) was put on  $Q_{\text{max}}$  (the Brillouin zone edge) to constrain it to the value calculated from the measured lattice parameter (Tables S1a and S2a). Individual spectra were modeled using a function that consisted of the sum of a double Lorentzian (one each for the Stokes and anti-Stokes phonon peaks), a pseudo-Voigt (for the elastic peak, when present), and a constant background (Figures S2a–S2c). Other than the strong constraint on the phonon position, all parameters were fit with a flat prior. The Markov chains corresponding to each fit exhibited high convergence and minimal autocorrelation over 25,000 samples.

The sound velocity corresponding to each phonon branch was determined from the slope of the fit sine function at the Brillouin zone center:

$$\text{slope}_{\text{zone\_center}} [\text{meV/nm}^{-1}] = 4.192 \times 10^{-4} \times \frac{\pi}{2} \times \text{velocity}_{\text{fit}} [\text{m/s}], \quad (2)$$

multiplied by a unit conversion factor, 1.519, to convert from meV/nm to km/s. The independent elastic stiffness moduli ( $C_{ij}$ 's) for cubic crystals,  $C_{11}$ ,  $C_{44}$ , and  $C_{12}$  were determined by combining the three measured sound velocities with the sample density. Additional quantities, such as isotropic velocities, isotropic elastic moduli, and velocity anisotropies, were calculated from the elastic stiffness tensor.

The sound velocities and corresponding elastic constants from our MgO sample were used to benchmark our fitting procedure and to compare our results with previous studies, as the elasticity of MgO has been studied extensively using a variety of techniques. We found that with our fitting method it was imperative to limit the maximum reduced Q to less than or equal to 0.2 (reduced Q =  $Q[\text{nm}^{-1}]/Q_{\text{max}}[\text{nm}^{-1}]$ ) to achieve velocities and elastic constants comparable to prior works. The minimum fit reduced Q reached a value as low as 0.03, which was made possible due to the high-energy resolution monochromator (Said et al., 2011; Toellner et al., 2011) and a single crystal with sharp diffraction peaks. Our choice to use a sine function to fit the phonon dispersions, as opposed to a linear function that is used in some single-crystal HERIX studies (e.g., Antonangeli et al., 2011; Lin et al., 2014), is justified by the discernable  $\sim 0.3$ -meV difference between the fit phonon energy at a reduced Q of 0.2 and a line with a slope equal to the slope of the fit sine function at the Brillouin zone center. This discrepancy continues to increase with higher Q values (Figure 2). Fitting all MgO acoustic phonon branches to a maximum reduced Q of 0.2 gives sound velocities of [100]  $V_p = 9.20(3)$ , [100]  $V_s = 6.59(3)$ , and [110]  $V_s = 5.408(17)$  km/s, which correspond to elastic stiffness constants of  $C_{11} = 302(3)$ ,  $C_{44} = 155.5(1.5)$ , and  $C_{12} = 93(3)$  GPa (using a measured lattice parameter of  $4.215 \text{ \AA}$  in the density calculation). These values are equivalent, within uncertainty, to those determined by Brillouin spectroscopy (Sinogeikin & Bass, 2000) and ultrasonic interferometry (Jacobsen et al., 2002; Table S2a). The dispersion curves are also consistent with previous inelastic neutron scattering measurements (Sangster et al., 1970; Figure 2).

For the [100] longitudinal acoustic and TA acoustic branches, where we collected data to a reduced Q of 0.6 and 1.0, respectively, if spectra were fit out to a maximum reduced Q of 0.6, sound velocities were found to be 2.5% ( $V_p$ ) or 3.3% ( $V_s$ ) lower than if they were fit out to only a maximum reduced Q of 0.2. This corresponds to discrepancies in the  $C_{11}$  and  $C_{44}$  elastic constants of 5.0% and 6.4% lower, respectively, and points to a more

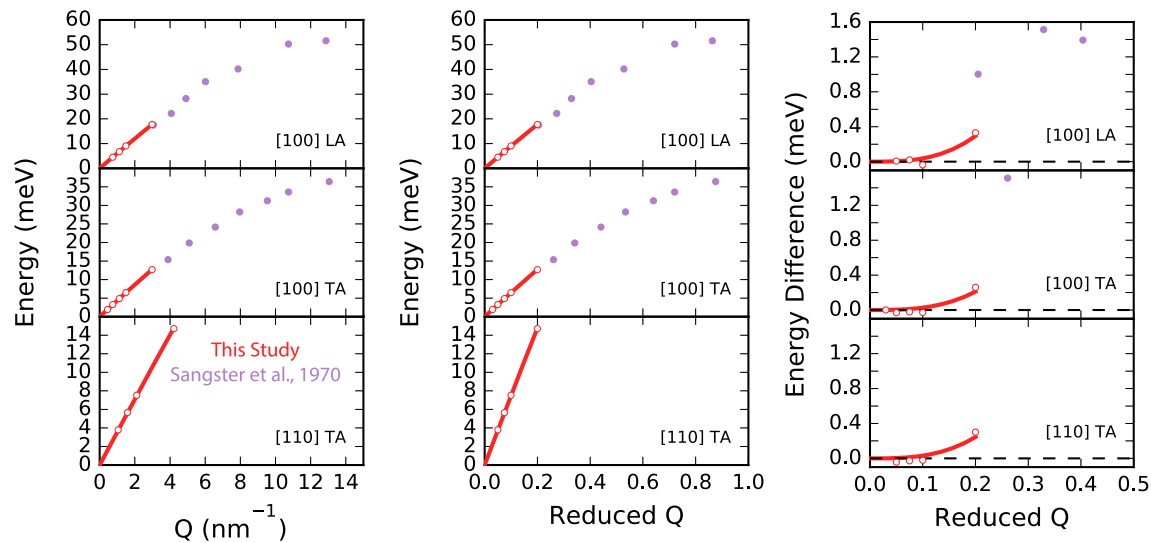


**Figure 2.** Left and center: MgO phonon dispersion relations at ambient conditions in terms of real (left) and reduced (center) momentum transfer,  $Q$ . The red-outlined circles show the individual fit phonon positions, and the solid red line indicates the sine function fit to the phonon dispersion. The purple circles represent points on the phonon dispersion determined from inelastic neutron scattering (Sangster et al., 1970; starting at a reduced  $Q$  of 0.20 for the [100] longitudinal acoustic phonon branch and 0.26 for the [100] transverse acoustic phonon branch). Note that the [110] transverse acoustic phonon dispersion has a steeper slope in reduced  $Q$  space than in absolute  $Q$  space relative to the [100] acoustic phonon dispersions. This is due to an additional scaling factor of  $\sqrt{2}$  for the [110] direction when converting from reduced  $Q$  to absolute  $Q$  space. Right: The red-outlined circles (individual fit phonon positions) and solid red line (fit sine function) show the deviation of the phonon dispersion from linearity (i.e., the difference between the phonon energy at a given momentum transfer and a line with a slope equivalent to that of the fit sine function at the Brillouin zone center). The dashed black line represents zero deviation from linearity.

complex dispersion relation than equation (1). If fit spectra were limited to a reduced  $Q$  range between 0.2 and 0.6, sound velocities were found to be 2.9% ( $V_p$ ) or 3.8% ( $V_s$ ) lower than if they were fit out to only a maximum reduced  $Q$  of 0.2, corresponding to a  $C_{11}$  and  $C_{44}$  that are 5.8% and 7.4% lower, respectively.

### 3.3. Inelastic X-Ray Scattering — (Mg,Fe)O

Considering the results from the MgO spectral fits, we limited the magnesiowüstite (Mw) spectra fit to those corresponding to reduced  $Q$  values less than or equal to 0.2. Spectra at low momentum transfers with phonons significantly overlapped by the elastic peak were also omitted from fitting (see supporting information). The minimum fit reduced  $Q$  was as low as 0.06. The spectra were fit in a similar manner to the MgO spectra, using the same fitting functions and constraints (see Figure 3 for example spectra at 2.8 GPa and Figures S2d–S2x for all fit spectra). Sound velocities were determined from the slope of the sine function at the Brillouin zone center (see Table S1b for sine function parameters and Figure 4 for dispersions), and elastic constants were determined by combining the sound velocities with measured densities (Table S2b).

The elastic constants of Mw are  $C_{11} = 237.0(1.7)$ ,  $C_{44} = 68.2(9)$ , and  $C_{12} = 122(3)$  GPa at ambient pressure, which are similar to those reported previously (Jacobsen et al., 2002) for the same batch of material (Figure 5). Between 0 and 10.5 GPa, the shear constants exhibit softening, with  $C_{12}$  exhibiting a flat slope and  $C_{44}$  decreasing to 46.4 GPa (see supporting information and Figure S2 for high-pressure sample configuration). The shear softening in  $C_{44}$  has been reported in prior publications (Jacobsen et al., 2004). Above this pressure, up to 35.4 GPa,  $C_{12}$  and  $C_{44}$  increase, while  $C_{11}$  increases steadily from ambient pressure. There is a measurable shift at the highest pressure measured, 41.2 GPa, where all three elastic constants exhibit softening. These trends are also present in the bulk modulus and shear modulus, as well as the corresponding isotropic sound velocities (Figure 6).

There is no evidence for a whole-crystal structural phase transformation at  $\sim 10$  GPa from the primary diffraction peaks of Mw, so the initial shear softening may be related to changes in the structure of the tetrahedrally coordinated ferric iron/oxygen defect clusters, as opposed to the bulk structure (see previous studies for further discussion of the [Mg,Fe]O defect structure; e.g., Finkelstein et al., 2017, and references therein). However, the SMS are virtually unchanged up to 34 GPa (Figure 1), and any changes related to the small

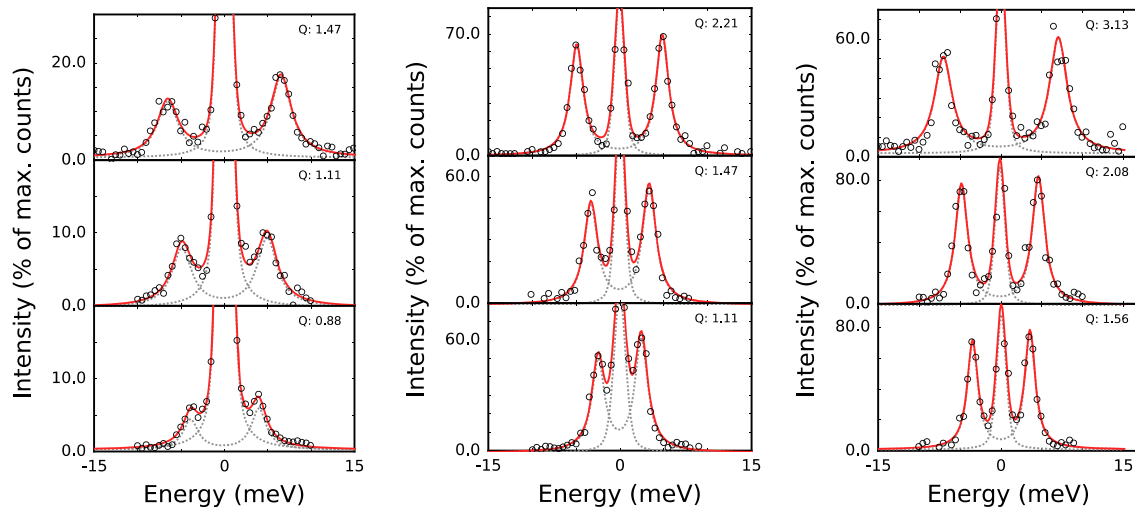


**Figure 3.** Magnesiowüstite HERIX spectra collected at 2.8 GPa corresponding to the [100] longitudinal (left), [100] transverse (center), and [110] transverse (right) acoustic modes. The black circles show the raw HERIX data, the red line represents the complete fit to a spectrum, and the gray dotted line illustrates individual components of the fit. HERIX = high-energy resolution inelastic X-ray.

amount (4.7 mol %) of ferric iron in the structure may not be detectable in a narrow delay time window. In contrast, the softening occurring at higher pressures correlates well with a noticeable increase in a broadened component in the Mössbauer spectra at similar pressures. This feature precedes a magnetic ordering transition between 50 and 64 GPa, while the structure remains cubic up to at least 55 GPa (Finkelstein et al., 2017), significantly higher than that for wüstite. The softening we observe around 34 and 41 GPa is likely related to the magnetic ordering transition.

Sound velocities as a function of crystallographic direction and polarization were calculated using the Christoffel equation in the SVEC module of MINUTI (Sturhahn, 2017), and the minimum and maximum

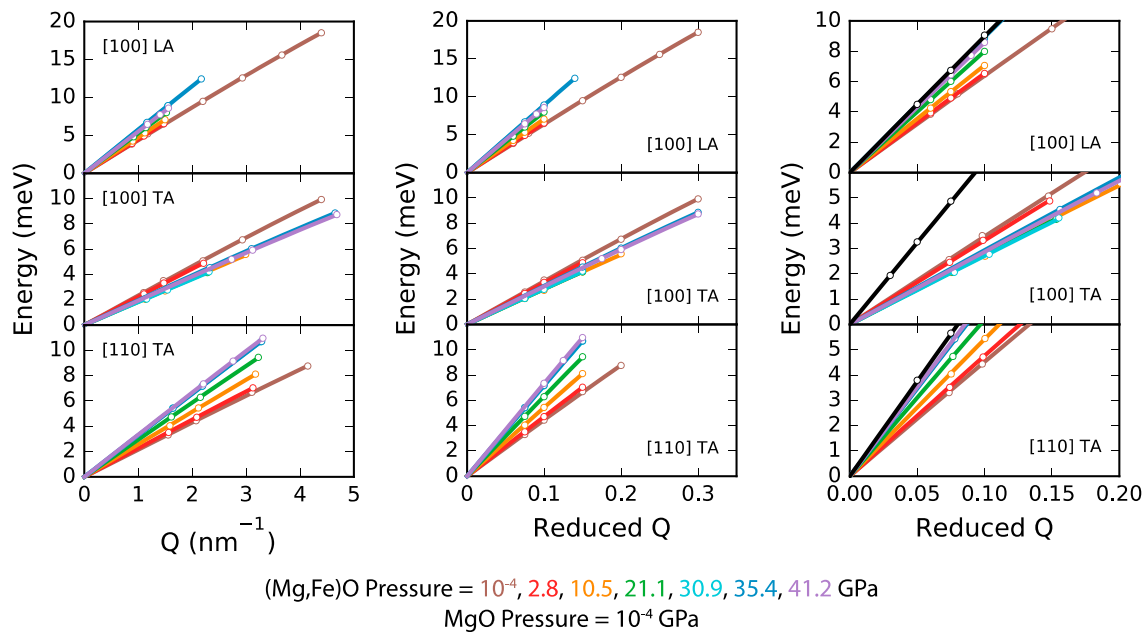


**Figure 4.** Left and center: Magnesiowüstite phonon dispersion relations at ambient and high pressures in terms of real (left) and reduced (center) momentum transfer,  $Q$ . The circles show the individual fit phonon positions, and the solid lines indicate the sine function fits to the phonon dispersions. Right: A magnified view of the magnesiowüstite phonon dispersions, with ambient-pressure MgO dispersion relations for comparison.

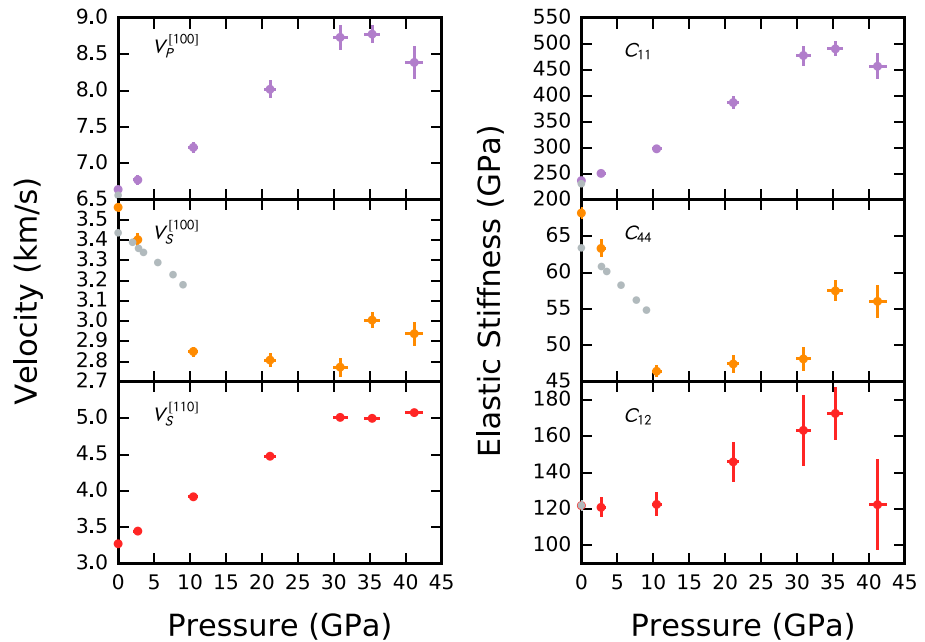


**Figure 5.** Left: Magnesiowüstite sound velocities as a function of pressure. Colored symbols are from this study, and gray symbols are from gigahertz ultrasonic interferometry measurements (Jacobsen et al., 2002, 2004). Right: Elastic stiffness moduli as a function of pressure, determined using sound velocities and densities.

velocity directions and magnitudes were identified (Figure 7 and Tables S3a and S3b). The  $V_p$  and  $V_s$  peak anisotropies were calculated according to

$$\text{Anisotropy (\%)} = 100 * \frac{V_{\max} - V_{\min}}{\left(\frac{V_{\max} + V_{\min}}{2}\right)} \quad (3)$$

Similar to low-iron (Mg,Fe)O compositions, the anisotropy of Mw decreases with increasing pressure until the fast and slow directions in the crystal switch, and at this point the crystal is elastically isotropic. In Mw, the anisotropy is initially relatively small (3.0%  $V_p$  and in 8.5%  $V_s$ ), and then decreases to near 0 at 2.8 GPa when the fast and slow directions switch. In low-iron concentrations, (Mg,Fe)O is isotropic around 18 GPa

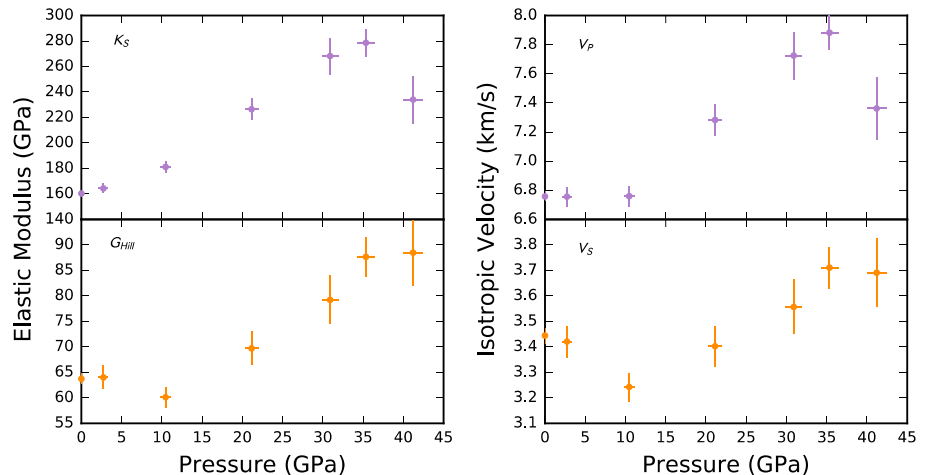


**Figure 6.** Left: Adiabatic bulk modulus ( $K_S$ ) and Voigt-Reuss-Hill shear modulus average ( $G_{RH}$ ) as a function of pressure calculated from elastic constants. Right: Isotropically averaged sound velocities calculated from  $K_S$ ,  $G_{RH}$ , and density.

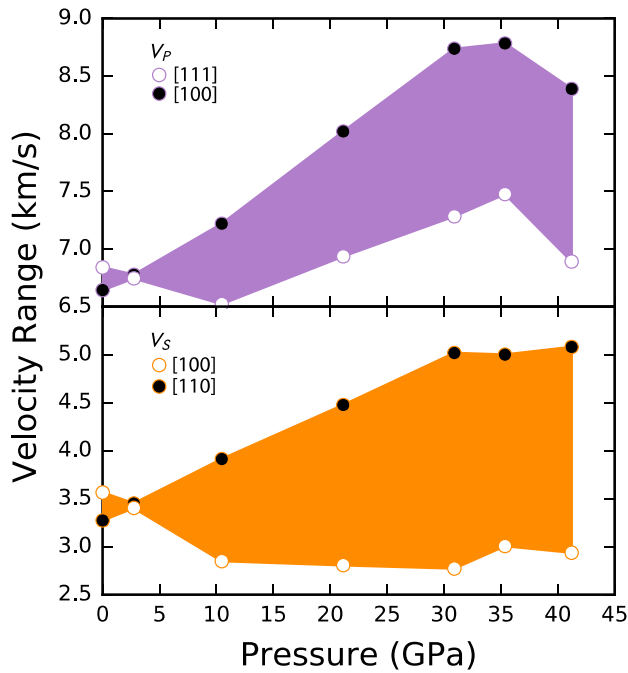


**Figure 7.** Velocity range for  $V_p$  (top) and  $V_s$  (bottom) as a function of pressure.

60% (Figure 8), suggesting that magnesiowüstite may provide a plausible alternative. This value is about 2.5 times higher than iron-poor (Mg,Fe)O compositions at similar pressures (Antonangeli et al., 2011; Marquardt et al., 2009) and about 2 to 3 times higher than magnesium- or iron-rich postperovskite at CMB conditions (e.g., Caracas, 2005; Stackhouse et al., 2005). While our measurements were conducted at room temperature, the addition of high temperature may increase the elastic anisotropy (Karki, 1999).

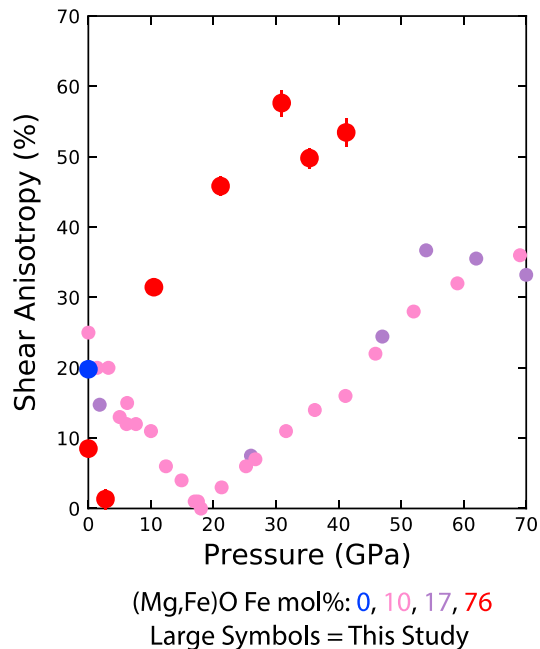


**Figure 8.** Shear anisotropy as a function of pressure. Large symbols show data (Mw and MgO) from this study. Data from (Mg,Fe)O samples with 10 mol % (Marquardt et al., 2009) and 17 mol % (Antonangeli et al., 2011) iron are shown with smaller symbols for comparison. Error bars are only plotted for results from this study.

(Marquardt et al., 2009). Above this pressure, however, the rate of anisotropy increase with pressure for Mw is significantly higher than in iron-poor (Mg,Fe)O or MgO, reaching a maximum of 19.6% and 57.6% in  $V_p$  and  $V_s$ , respectively (see Figure 8 for shear anisotropy).

#### 4. Discussion

Shear wave anisotropy has been observed in the vicinity of LLSVPs and interpreted as revealing complex flow occurring at the edges of LLSVPs (Cottaar & Romanowicz, 2013; Ford et al., 2015; Lynner & Long, 2014; Wang & Wen, 2007), suggesting strong interactions between the LLSVP and the surrounding mantle. Therefore, conditions may be optimal for alignment of crystallographic axes of elastically anisotropic minerals, thus providing a source of observed seismic anisotropy. Shear anisotropy values that have been reported for potential mantle phases include: 17% for  $\text{Fo}_{90.5}\text{Fa}_{9.5}$  olivine at 12.8 GPa and 1300 K (J. S. Zhang & Bass, 2016); 42% for MgO at 136 GPa and 3000 K (Karki, 1999); and 26–30% for  $\text{MgSiO}_3$  postperovskite at 136 GPa and 3000 K (Stackhouse et al., 2005), and  $\text{FeSiO}_3$  postperovskite at 120 GPa and 300 K (Caracas, 2005). Recent studies argue that  $\text{MgSiO}_3$  postperovskite is the primary candidate for the observed anisotropy (Ford et al., 2015; Miyagi et al., 2010); however, our results show that magnesiowüstite develops a shear anisotropy approaching

In some regions, the lowermost edges of LLSVPs exhibit patches of LVZ and ULVZ, from a few to tens of kilometers thick and ~100 km across (Garnero & Helmberger, 1995; Yu & Garnero, 2018), which may be linked to plume generation zones. These LVZs may be fossil remnants of large-scale melting events in the early Earth (Labrosse et al., 2007) and/or could form by reaction with the outer core (W. E. Jackson et al., 1987). Within the LVZs, velocities of seismic waves are reduced by ~5% to 30% (Garnero & Helmberger, 1995; Hutko et al., 2009; Mori & Helmberger, 1995). Only partial melting and/or extreme chemical and phase heterogeneity could explain such features (Muir & Brodholt, 2015; Wicks et al., 2017).

It has yet to be conclusively determined if LVZs are solid or partially molten structures. A partial melt origin for ultra-LVZs predicts a  $P$  to  $S$  wave speed reduction of about 1:3 (Williams & Garnero, 1996). In this scenario, the velocities of the average assemblage are decreased by melt formed by chemical reaction of the iron-rich liquid outer core with the solid silicate-rich mantle and/or by partial melting of the mantle. The hypothesis is consistent with the correlation between ultra-LVZs and hot spots (Williams et al., 1998); however, very few studies constrain the  $P$  and  $S$  wave speeds in the same location. While early dynamical calculations questioned the ability to produce a dense and nonpercolating melt phase in the deep Earth, a later study showed that the stirring of LVZs by the larger-scale convective motions of the mantle can potentially maintain partially molten regions (Hernlund &

Jellinek, 2010). However, shock wave measurements that constrained the densities of iron-bearing silicate liquids suggest that for a range of mantle compositions, partial melts of these petrologic assemblages would not be dense enough to remain at the CMB on geologic timescales (Thomas & Asimow, 2013).

We hypothesize that magnesiowüstite has accumulated in patches at the base of the mantle, some near the edges of LLSVPs, and could be the primary control on observed seismic (isotropic and anisotropic) characteristics. Although recent studies point to postperovskite as the primary candidate for explaining such anisotropy near the base of the mantle (Ford et al., 2015; Stackhouse et al., 2005; Wentzcovitch et al., 2006), environments with elevated temperatures may inhibit the postperovskite transition (Hirose, 2006; Shim, 2008). Provided that the temperatures are below magnesiowüstite's solidus, the preferred alignment of magnesiowüstite in the lowermost mantle could be an alternative or an additional source of seismic anisotropy. Future work is needed to explore the active slip systems in magnesiowüstite at lower-mantle conditions and also the effect of deformation partitioning between silicate postperovskite and magnesiowüstite, as there is evidence from studies on (ferro)periclase that the magnitude of seismic anisotropy originating from magnesiowüstite would be sensitive to both (Girard et al., 2012; Immoor et al., 2018; Marquardt & Miyagi, 2015; Yamazaki et al., 2014).

#### Acknowledgments

We thank Stephen J. Mackwell for providing the single crystals for this study and Rachel A. Morrison for help in conducting experiments. We are thankful to NSF-CSEDI-EAR-1161046 and 1600956, the W. M. Keck Institute for Space Studies for financial support, and two anonymous reviewers for their helpful comments. G. J. Finkelstein is also partially supported by the Caltech Seismological Laboratory Director's Postdoctoral Fellowship. We acknowledge COMPRES for partial support of Sector 3 and Sector 30 at the Advanced Photon Source (APS). Ruby fluorescence measurements were conducted at GSECARS, which is supported by NSF-EAR-1128799 and U.S. DOE, Geosciences (DE-FG02-94ER14466. Use of the APS is supported by U.S. DOE, Office of Science (DE-AC02-06CH11357). The spectra corresponding to the results reported in this paper are provided in the supporting information.

#### References

- Antonangeli, D., Siebert, J., Aracne, C. M., Farber, D. L., Bosak, A., Hoesch, M., et al. (2011). Spin crossover in ferropericlase at high pressure: A seismologically transparent transition? *Science*, *331*(6013), 64–67. <https://doi.org/10.1126/science.1198429>
- Boehler, R., & De Hantsetters, K. (2007). New anvil designs in diamond-cells. *High Pressure Research*, *24*, 391–396.
- Bower, D. J., Wicks, J. K., Gurnis, M., & Jackson, J. M. (2011). A geodynamic and mineral physics model of a solid-state ultralow-velocity zone. *Earth and Planetary Science Letters*, *303*, 193–202.
- Caracas, R. (2005). Effect of chemistry on the stability and elasticity of the perovskite and post-perovskite phases in the MgSiO<sub>3</sub>-FeSiO<sub>3</sub>-Al<sub>2</sub>O<sub>3</sub> system and implications for the lowermost mantle. *Geophysical Research Letters*, *32*, L16310. <https://doi.org/10.1029/2005GL023164>
- Cottaar, S., & Romanowicz, B. (2013). Observations of changing anisotropy across the southern margin of the African LLSVP. *Geophysical Journal International*, *195*(2), 1184–1195. <https://doi.org/10.1093/gji/ggt285>
- Crowhurst, J. C., Brown, J. M., Goncharov, A. F., & Jacobsen, S. D. (2008). Elasticity of (Mg,Fe) O through the spin transition of iron in the lower mantle. *Science*, *319*(5862), 451–453. <https://doi.org/10.1126/science.1149606>
- Dewaele, A., Loubeyre, P., & Mezouar, M. (2004). Equations of state of six metals above 94 GPa. *Physical Review B*, *70*(9), 094112. <https://doi.org/10.1103/PhysRevB.70.094112>
- Dorfman, S. M., & Duffy, T. S. (2014). Effect of Fe-enrichment on seismic properties of perovskite and post-perovskite in the deep lower mantle. *Geophysical Journal International*, *197*(2), 910–919. <https://doi.org/10.1093/gji/ggu045>
- Finkelstein, G. J., Jackson, J. M., Sturhahn, W., Zhang, D., Alp, E. E., & Toellner, T. S. (2017). Single-crystal equations of state of magnesiowüstite at high pressures. *American Mineralogist*, *102*(8), 1709–1717. <https://doi.org/10.2138/am-2017-5966>
- Fiquet, G., Badro, J., Gregoryanz, E., Fei, Y., & Occelli, F. (2009). Sound velocity in iron carbide (Fe<sub>3</sub>C) at high pressure: Implications for the carbon content of the Earth's inner core. *Physics of the Earth and Planetary Interiors*, *172*(1–2), 125–129. <https://doi.org/10.1016/j.pepi.2008.05.016>
- Ford, H. A., Long, M. D., He, X., & Lynner, C. (2015). Lowermost mantle flow at the eastern edge of the African Large Low Shear Velocity Province. *Earth and Planetary Science Letters*, *420*, 12–22. <https://doi.org/10.1016/j.epsl.2015.03.029>
- Frost, D. A., Garnero, E. J., & Rost, S. (2018). Dynamical links between small- and large-scale mantle heterogeneity: Seismological evidence. *Earth and Planetary Science Letters*, *482*, 135–146. <https://doi.org/10.1016/j.epsl.2017.10.058>
- Frost, D. A., Rost, S., Garnero, E. J., & Li, M. (2017). Seismic evidence for Earth's crusty deep mantle. *Earth and Planetary Science Letters*, *470*, 54–63. <https://doi.org/10.1016/j.epsl.2017.04.036>
- Garnero, E. J., & Helmberger, D. V. (1995). A very slow basal layer underlying large-scale low-velocity anomalies in the lower mantle beneath the Pacific: Evidence from core phases. *Physics of the Earth and Planetary Interiors*, *91*(1–3), 161–176. [https://doi.org/10.1016/0031-9201\(95\)03039-Y](https://doi.org/10.1016/0031-9201(95)03039-Y)
- Garnero, E. J., & Helmberger, D. V. (1998). Further structural constraints and uncertainties of a thin laterally varying ultralow-velocity layer at the base of the mantle. *Journal of Geophysical Research*, *103*(B6), 12,495–12,509. <https://doi.org/10.1029/98JB00700>
- Girard, J., Chen, J., & Raterron, P. (2012). Deformation of periclase single crystals at high pressure and temperature: Quantification of the effect of pressure on slip-system activities. *Journal of Applied Physics*, *111*(11), 112607. <https://doi.org/10.1063/1.4726200>
- Hernlund, J. W., & Jellinek, A. M. (2010). Dynamics and structure of a stirred partially molten ultralow-velocity zone. *Earth and Planetary Science Letters*, *296*(1–2), 1–8. <https://doi.org/10.1016/j.epsl.2010.04.027>
- Hirose, K. (2006). Postperovskite phase transition and its geophysical implications. *Reviews of Geophysics*, *44*, RG3001. <https://doi.org/10.1029/2005RG000186>
- Hutko, A. R., Lay, T., & Revenaugh, J. (2009). Localized double-array stacking analysis of PcP: D and ULVZ structure beneath the Cocos plate, Mexico, central Pacific, and North Pacific. *Physics of the Earth and Planetary Interiors*, *173*(1–2), 60–74. <https://doi.org/10.1016/j.pepi.2008.11.003>
- Immoor, J., Marquardt, H., Miyagi, L., Lin, F., Speziale, S., Merkel, S., et al. (2018). Evidence for {100}<011> slip in ferropericlase in Earth's lower mantle from high-pressure/high-temperature experiments. *Earth and Planetary Science Letters*, *489*, 251–257. <https://doi.org/10.1016/j.epsl.2018.02.045>
- Jackson, J. M., Sinogeikin, S. V., Jacobsen, S. D., Reichmann, H. J., Mackwell, S. J., & Bass, J. D. (2006). Single-crystal elasticity and sound velocities of (Mg<sub>0.94</sub>Fe<sub>0.06</sub>) O ferropericlase to 20 GPa. *Journal of Geophysical Research*, *111*, B09203. <https://doi.org/10.1029/2005JB004052>
- Jackson, W. E., Knittle, E., Brown, G. E. Jr., & Jeanloz, R. (1987). Partitioning of Fe within high-pressure silicate perovskite: Evidence for unusual geochemistry in the lower mantle. *Geophysical Research Letters*, *14*(3), 224–226. <https://doi.org/10.1029/GL014i003p00224>

- Jacobsen, S. D., Reichmann, H. J., Spetzler, H. A., Mackwell, S. J., Smyth, J. R., Angel, R. J., & McCammon, C. A. (2002). Structure and elasticity of single-crystal (Mg,Fe)O and a new method of generating shear waves for gigahertz ultrasonic interferometry. *Journal of Geophysical Research*, 107(B2), 2037. <https://doi.org/10.1029/2001JB000490>
- Jacobsen, S. D., Spetzler, H., Reichmann, H. J., & Smyth, J. R. (2004). Shear waves in the diamond-anvil cell reveal pressure-induced instability in (Mg,Fe)O. *Proceedings of the National Academy of Sciences of the United States of America*, 101, 5867–5871.
- Kantor, I., Prakapenka, V., Kantor, A., Dera, P., Kurnosov, A., Sinogeikin, S., et al. (2012). BX90: A new diamond anvil cell design for X-ray diffraction and optical measurements. *Review of Scientific Instruments*, 83(12), 125102. <https://doi.org/10.1063/1.4768541>
- Karki, B. B. (1999). First-principles determination of elastic anisotropy and wave velocities of MgO at lower mantle conditions. *Science*, 286(5445), 1705–1707. <https://doi.org/10.1126/science.286.5445.1705>
- Knittle, E., & Jeanloz, R. (1986). High-pressure metallization of FeO and implications for the Earth's core. *Geophysical Research Letters*, 13(13), 1541–1544. <https://doi.org/10.1029/GL013i013p01541>
- Labrosse, S., Hernlund, J. W., & Coltice, N. (2007). A crystallizing dense magma ocean at the base of the Earth's mantle. *Nature*, 450(7171), 866–869. <https://doi.org/10.1038/nature06355>
- Li, M., McNamara, A. K., Garnero, E. J., & Yu, S. (2017). Compositionally-distinct ultra-low velocity zones on Earth's core-mantle boundary. *Nature Communications*, 8, 977.
- Lin, J.-F., Wu, J., Zhu, J., Mao, Z., Said, A. H., Leu, B. M., et al. (2014). Abnormal elastic and vibrational behaviors of magnetite at high pressures. *Scientific Reports*, 4, 6282.
- Lynner, C., & Long, M. D. (2014). Lowermost mantle anisotropy and deformation along the boundary of the African LLSVP. *Geophysical Research Letters*, 41, 3447–3454. <https://doi.org/10.1002/2014GL059875>
- Mao, W. L., Shen, G., Prakapenka, V. B., Meng, Y., Campbell, A. J., Heinz, D. L., et al. (2004). Ferromagnesian postperovskite silicates in the D layer of the Earth. *Proceedings of the National Academy of Sciences of the United States of America*, 101, 15,867–15,869.
- Marquardt, H., & Miyagi, L. (2015). Slab stagnation in the shallow lower mantle linked to an increase in mantle viscosity. *Nature Geoscience*, 8(4), 311–314. <https://doi.org/10.1038/ngeo2393>
- Marquardt, H., Speziale, S., Reichmann, H. J., Frost, D. J., Schilling, F. R., & Garnero, E. J. (2009). Elastic shear anisotropy of ferropericline in Earth's lower mantle. *Science*, 324(5924), 224–226. <https://doi.org/10.1126/science.1169365>
- McNamara, A. K., van Keken, P. E., & Karato, S.-I. (2002). Development of anisotropic structure in the Earth's lower mantle by solid-state convection. *Nature*, 416(6878), 310–314. <https://doi.org/10.1038/416310a>
- Miyagi, L., Kanitpanyacharoen, W., Kaercher, P., Lee, K. K. M., & Wenk, H. R. (2010). Slip systems in MgSiO<sub>3</sub> post-perovskite: Implications for D anisotropy. *Science*, 329(5999), 1639–1641. <https://doi.org/10.1126/science.1192465>
- Mori, J., & Helmberger, D. V. (1995). Localized boundary layer below the mid-Pacific velocity anomaly identified from a PcP precursor. *Journal of Geophysical Research*, 100(B10), 20,359–20,365. <https://doi.org/10.1029/95JB02243>
- Muir, J. M. R., & Brodholt, J. P. (2015). Elastic properties of ferropericline at lower mantle conditions and its relevance to ULVZs. *Earth and Planetary Science Letters*, 417, 40–48. <https://doi.org/10.1016/j.epsl.2015.02.023>
- Oganov, A. R., Martoňák, R., Laio, A., Raiteri, P., & Parrinello, M. (2005). Anisotropy of Earth's D layer and stacking faults in the MgSiO<sub>3</sub> post-perovskite phase. *Nature*, 438(7071), 1142–1144. <https://doi.org/10.1038/nature04439>
- Said, A. H., Sinn, H., & Divan, R. (2011). New developments in fabrication of high-energy-resolution analyzers for inelastic X-ray spectroscopy. *Journal of Synchrotron Radiation*, 18(3), 492–496. <https://doi.org/10.1107/S0909049511001828>
- Sakai, T., Ohtani, E., Terasaki, H., Miyahara, M., Nishijima, M., Hirao, N., et al. (2009). Fe–Mg partitioning between post-perovskite and ferropericline in the lowermost mantle. *Physics and Chemistry of Minerals*, 37, 487–496.
- Sakamaki, T., Ohtani, E., Fukui, H., Kamada, S., Takahashi, S., Sakairi, T., et al. (2016). Constraints on Earth's inner core composition inferred from measurements of the sound velocity of hcp-iron in extreme conditions. *Science Advances*, 2, 1–6.
- Salvatier, J., Wiecki, T. V., & Fonnesbeck, C. (2016). Probabilistic programming in Python using PyMC3. *PeerJ Computer Science*, 2, e55. <https://doi.org/10.7717/peerj-cs.55>
- Sangster, M. J. L., Peckham, G., & Saunderson, D. H. (1970). Lattice dynamics of magnesium oxide. *Journal of Physics C: Solid State Physics*, 3(5), 1026–1036. <https://doi.org/10.1088/0022-3719/3/5/017>
- Shim, S.-H. (2008). The postperovskite transition. *Annual Review of Earth and Planetary Sciences*, 36(1), 569–599. <https://doi.org/10.1146/annurev.earth.36.031207.124309>
- Sinn, H. (2001). Spectroscopy with meV energy resolution. *Journal of Physics: Condensed Matter*, 13, 7525–7537.
- Sinogeikin, S. V., & Bass, J. D. (2000). Single-crystal elasticity of pyrope and MgO to 20 GPa by Brillouin scattering in the diamond cell. *Physics of the Earth and Planetary Interiors*, 120(1–2), 43–62. [https://doi.org/10.1016/S0031-9201\(00\)00143-6](https://doi.org/10.1016/S0031-9201(00)00143-6)
- Stackhouse, S., Brodholt, J. P., Wookey, J., Kendall, J. M., & Price, G. D. (2005). The effect of temperature on the seismic anisotropy of the perovskite and post-perovskite polymorphs of MgSiO<sub>3</sub>. *Earth and Planetary Science Letters*, 230(1–2), 1–10. <https://doi.org/10.1016/j.epsl.2004.11.021>
- Sturhahn, W. (2004). Nuclear resonant spectroscopy. *Journal of Physics: Condensed Matter*, 16, S497–S530.
- Sturhahn, W. (2017). MINUTI (MINeral physics UTILities) and PHOENIX (PHOnon Excitation by Nuclear Inelastic X-ray scattering) open source software. Retrieved from [www.nrxs.com](http://www.nrxs.com)
- Thomas, C. W., & Asimow, P. D. (2013). Direct shock compression experiments on premolten forsterite and progress toward a consistent high-pressure equation of state for CaO–MgO–Al<sub>2</sub>O<sub>3</sub>–SiO<sub>2</sub>–FeO liquids. *Journal of Geophysical Research: Solid Earth*, 118, 5738–5752. <https://doi.org/10.1002/jgrb.50374>
- Toellner, T. S., Alatas, A., & Said, A. H. (2011). Six-reflection meV-monochromator for synchrotron radiation. *Journal of Synchrotron Radiation*, 18(4), 605–611. <https://doi.org/10.1107/S0909049511017535>
- Townsend, J. P., Tsuchiya, J., Bina, C. R., & Jacobsen, S. D. (2016). Water partitioning between bridgmanite and postperovskite in the lowermost mantle. *Earth and Planetary Science Letters*, 454, 20–27. <https://doi.org/10.1016/j.epsl.2016.08.009>
- Wang, Y., & Wen, L. (2007). Complex seismic anisotropy at the border of a very low velocity province at the base of the Earth's mantle. *Journal of Geophysical Research*, 112, B09305. <https://doi.org/10.1029/2006JB004719>
- Wentzcovitch, R. M., Tsuchiya, T., & Tsuchiya, J. (2006). MgSiO<sub>3</sub> postperovskite at D conditions. *Proceedings of the National Academy of Sciences of the United States of America*, 103, 543–546.
- Wicks, J. K., Jackson, J. M., & Sturhahn, W. (2010). Very low sound velocities in iron-rich (Mg,Fe)O: Implications for the core-mantle boundary region. *Geophysical Research Letters*, 37, L15304. <https://doi.org/10.1029/2010GL043689>
- Wicks, J. K., Jackson, J. M., Sturhahn, W., & Zhang, D. (2017). Sound velocity and density of magnesio-wüstites: Implications for ultralow-velocity zone topography. *Geophysical Research Letters*, 44, 2148–2158. <https://doi.org/10.1002/2016GL071225>
- Williams, Q., & Garnero, E. J. (1996). Seismic evidence for partial melt at the base of Earth's mantle. *Science*, 273(5281), 1528–1530. <https://doi.org/10.1126/science.273.5281.1528>

- Williams, Q., Revenaugh, J., & Garnero, E. (1998). A correlation between ultra-low basal velocities in the mantle and hot spots. *Science*, 281(5376), 546–549. <https://doi.org/10.1126/science.281.5376.546>
- Wu, X., Lin, J.-F., Kaercher, P., Mao, Z., Liu, J., Wenk, H.-R., & Prakapenka, V. B. (2017). Seismic anisotropy of the D layer induced by (001) deformation of post-perovskite. *Nature Communications*, 8, 14,669. <https://doi.org/10.1038/ncomms14669>
- Yamazaki, D., Yoshino, T., & Nakakuki, T. (2014). Interconnection of ferro-periclase controls subducted slab morphology at the top of the lower mantle. *Earth and Planetary Science Letters*, 403, 352–357. <https://doi.org/10.1016/j.epsl.2014.07.017>
- Yu, S., & Garnero, E. J. (2018). Ultralow velocity zone locations: A global assessment. *Geochemistry, Geophysics, Geosystems*, 19, 396–414. <https://doi.org/10.1002/2017GC007281>
- Zhang, B., Ni, S., Sun, D., Shen, Z., Jackson, J. M., & Wu, W. (2018). Constraints on small-scale heterogeneity in the lowermost mantle from observations of near podal PcP precursors. *Earth and Planetary Science Letters*, 489, 267–276. <https://doi.org/10.1016/j.epsl.2018.01.033>
- Zhang, J. S., & Bass, J. D. (2016). Sound velocities of olivine at high pressures and temperatures and the composition of Earth's upper mantle. *Geophysical Research Letters*, 43, 9611–9618. <https://doi.org/10.1002/2016GL069949>